Numerical simulation of shear-induced instabilities in internal solitary waves

MAGDA CARR†, STUART E. KING AND DAVID G. DRITSCHEL

School of Mathematics and Statistics, University of St Andrews, Fife, KY16 9SS, UK.

(Received)

A numerical method that employs a combination of contour advection and pseudo-spectral techniques is used to simulate shear-induced instabilities in an internal solitary wave. A three-layer configuration for the background stratification in which a linearly stratified intermediate layer is sandwiched between two homogeneous ones is considered throughout. The flow is assumed to satisfy the inviscid, incompressible, Oberbeck-Boussinesq equations in two dimensions. Simulations are initialized by fully nonlinear, steady state, internal solitary waves. The results of the simulations show that the instability takes place in the pycnocline and manifests itself as Kelvin-Helmholtz billows. The billows form near the trough of the wave, subsequently grow and disturb the tail. Both the critical Richardson number (Ri_c) and the critical amplitude required for instability are found to be functions of the ratio of the undisturbed layer thicknesses. It is shown, therefore, that the constant, critical bound for instability in ISWs given in Barad & Fringer (2010), namely $Ri_c = 0.1 \pm 0.01$, is not a sufficient condition for instability. It is also shown that the critical value of L_x/λ required for instability, where L_x is the length of the region in a wave in which $Ri < 1/4$ and λ is the half width of the wave, is sensitive to the ratio of the layer thicknesses. Similarly, a linear stability analysis reveals

† Email address for correspondence: magda@mcs.st-and.ac.uk

that, $\bar{\sigma}_i T_w$, where $\bar{\sigma}_i$ is the growth rate of the instability averaged over T_w, the period in which parcels of fluid are subjected to $Ri < 1/4$, is very sensitive to the transition between the undisturbed pycnocline and the homogeneous layers and, the amplitude of the wave. Therefore, the alternative tests for instability presented in Fructus *et al.* (2009) and Barad & Fringer (2010), respectively, namely $L_x/\lambda \geqslant 0.86$ and $\bar{\sigma}_i T_w > 5$, are shown to be valid only for a limited parameter range.

1. Introduction

Internal solitary waves (ISWs) are ubiquitous features in the Earth's atmosphere and ocean. See the recent reviews by Apel *et al.* (2006), Grue (2006), Helfrich & Melville (2006) and Apel *et al.* (2007), for a thorough review of past and present work in the field. In the open ocean, typically, the waves are highly nonlinear and may attain very large amplitudes, for example in water depths of 200-300m they are frequently observed as waves of depression having amplitudes of up to 120m. It is well known that shear-induced instabilities can occur in large amplitude ISWs. For example they have been seen in the field (Moum *et al.* 2003), the laboratory (Fructus *et al.* 2009) and in numerical simulations (Barad & Fringer 2010).

Breaking ISWs can result in vertical mixing in the environment in which they propagate. They are an important source of mixing, turbulence, re-distribution of potential energy in the water column and mass and momentum transfer. In physical oceanography, one of the most topical issues of debate is the role of internal waves on the overall mixing of coastal oceans - a process that, in turn, has implications for global ocean circulation, heat transport and hence climate modelling, see Munk & Wunsch (1998), Garrett (2003*a*), Garrett (2003*b*), Thorpe (2004), Munk & Bills (2007) and Schiermeier (2007). ISWs can present significant hazards in coastal and oceanic regions where off-

shore petroleum exploration, production and sub-sea storage activities are in progress, for example see Osborne *et al.* (1978) and Osborne & Burch (1980). In addition, mixing induced by internal waves redistributes nutrients and dissolved gases, thus affecting biological productivity in the oceans. To understand the behaviour of ISWs in these contexts, it is imperative that the evolutionary processes which lead to breaking and the subsequent generation of turbulence be better understood.

Due to the difference in scale at which breaking is thought to take place and the scale at which large amplitude ISWs have been sampled, very limited field data are available for reference. Observations can be found in Woods (1968), Armi & Farmer (1988), Marmorino (1990) and van Haren & Gostiaux (2010). However, the cleanest observation of a breaking ISW is that of Moum *et al.* (2003). Figure 14 of their work shows an acoustical backscatter image of what appears to be a clear manifestation of a shear-induced (Kelvin-Helmholtz) instability in an ISW propagating shoreward over the Oregon continental shelf. The cause of the instability captured by Moum *et al.* (2003) is conjectured to be background shear, but questions concerning this cause remain open. In an effort to better understand such breaking in particular and instability in general, a numerical scheme that can simulate shear instabilities in ISWs is developed and presented here.

To study the evolution of an unstable ISW, two numerical schemes are employed. The first, outlined in King *et al.* (2010), is an iterative procedure to find a fully nonlinear steady state ISW solution. It takes any smooth profile of Brunt-Väisälä frequency squared as input and can compute significantly larger amplitude waves than have been presented elsewhere. The computations in King *et al.* (2010) do not appear to be limited by low Richardson number, unlike other routines that follow Turkington *et al.* (1991), for example see Lamb (2002). This is a key advantage in this study, as it is already well known that small Richardson numbers, well below 1/4, are required for instability in

ISWs (Fructus *et al.* 2009; Barad & Fringer 2010). The second numerical scheme, outlined in Dritschel & Fontane (2010), takes a steady state solution as input and evolves it with time. The method which has been termed the Combined Lagrangian Advection Method (CLAM) uses a combination of contour advection (Dritschel & Ambaum 1997) and standard pseudo-spectral techniques. Importantly, CLAM requires no numerical diffusion of density to maintain numerical stability. A detailed discussion of the accuracy of the method can be found in Fontane & Dritschel (2009). Application of the numerical model in the context of breaking ISWs is novel. The stability of an ISW propagating in an undisturbed stratification consisting of a linearly stratified middle layer sandwiched between homogeneous top and bottom layers is focused upon here. Note that no perturbations (or noise) are added to the initial state to trigger instability. A wide sweep of parameter space is performed and significant new findings are obtained as a result.

The only other numerical scheme in the literature that has been used to simulate shear-induced instabilities in ISWs in a similar stratification is the recent work of Barad & Fringer (2010). They used an adaptive numerical method to simulate instabilities in open-ocean ISWs. Their numerical scheme solves the Navier-Stokes equation in two dimensions and resolves all of the length scales of interest by dynamically tracking important regions with recursively-nested finer grids. Barad & Fringer (2010) focused on simulating waves similar to those that were observed by Moum *et al.* (2003). In particular, they concentrated on simulating the instabilities along the pycnocline that Moum *et al.* (2003) were unable to resolve with their measurements. They claimed that a sufficient criterion for instability was that the Richardson number in the wave must fall below a critical value of $Ri_c = 0.1 \pm 0.01$. However, they considered a very limited parameter space. They only presented 12 simulations and focused specifically on 9 of them. In particular, they assessed the effects of the non-dimensional interface thickness on the critical

amplitude and Richardson number for instability and kept all other parameters fixed. In this paper, a much wider parameter space is investigated. The ratio of all three layer depths and the smoothness of transition between layers are varied. It is found that the stability of the system is very sensitive to changes in these parameters and in particular, that the critical Richardson number required for instability is a function of these parameters. Hence it is shown that a constant $Ri_c = 0.1 \pm 0.01$ is not a sufficient condition for assessing instability in ISWs. In particular, it is shown that if the thickness of the lower layer is greater than approximately nine times the thickness of the upper two layers added together then the critical Richardson number required for instability is less than 0.09. Moreover, if the thickness of the lower layer is less than approximately five times the thickness of the upper two layers added together then the critical Richardson number required for instability is larger than 0.11 (see §4.2 figure 13).

In Fructus *et al.* (2009), experimental observations of stable and unstable waves, propagating in a stratification similar to that studied here were presented. In addition, numerical calculations for fully nonlinear steady states were made. It was reported that breaking waves occurred for amplitudes above a critical threshold of $a_1 = 2.24\sqrt{h_1 h_2}(1 + h_2/h_1)$ when $h_2/h_1 < 1$, where h_1 and h_2 are the thicknesses of the undisturbed top and middle layers respectively, and a_1 is the maximum displacement of an isopycnal that traces the upper interface of the pycnocline. In Fructus *et al.* (2009), the non dimensional thickness of the lower layer, $h_3/(h_1 + h_2)$, varied between 3.22 and 7.25 but no account of this variation was made. It is shown here that the critical amplitude marking the threshold between stability and instability is dependent on both h_2/h_1 and $h_3/(h_1+h_2)$, and hence the bound given in Fructus *et al.* (2009) should be used with caution. Fructus *et al.* (2009) also presented a stability bound based on L_x/λ, where L_x is the length of the region in a wave in which $Ri < 1/4$ and λ is the half width of the wave. They found that instability

required a value of $L_x/\lambda \geqslant 0.86$. The computations in Barad & Fringer (2010) agree with this bound. It will be shown here, that the critical value of L_x/λ required for instability is sensitive to the ratio of the layer depths and the bounds given in Fructus *et al.* (2009) and Barad & Fringer (2010) are only valid within a limited parameter range.

During the final stages of the submission process of this paper, the authors were made aware of a recently submitted manuscript by Lamb & Farmer (2011) that presents numerical simulations specifically designed to explore the mechanisms responsible for instability observed in an internal solitary-like wave. The observed wave was acquired in the same area and during the same period as the observations discussed in Moum *et al.* (2003). The model background stratification was closely matched to the observed density profile ahead of the wave and it was found that instabilities occurred when (i) the minimum Richardson number in the pycnocline was less than about 0.1; (ii) $L_x/\lambda > 0.8$; and (iii) a linear stability analysis predicted $\ln(a_f/a_i) >\approx 4$, where a_i and a_f are the amplitudes of perturbations entering and leaving the unstable region respectively. The numerical findings are in good agreement with the predictions of Fructus *et al.* (2009) and Barad & Fringer (2010). However, the objective of Lamb & Farmer (2011) was to simulate a particular observed wave. No variation of the background stratification was made which is the focus of the work presented here.

The physical interpretation of a bound based on L_x/λ is that unstable modes need some time in which to grow before breaking is observed (Fructus *et al.* 2009; Barad & Fringer 2010). This has also been observed in progressive interfacial gravity waves (Troy & Koseff 2005). In this paper, ISWs are classified into three different types: stable, weakly unstable and unstable. Weakly unstable waves are defined to be waves that exhibit oscillations on the pycnocline and either no coherent billows form or short lived billows occur but quickly collapse. These waves clearly have unstable modes associated with them but the

modes do not have sufficient time to grow into the persistent coherent billows seen in unstable waves. Stability curves are presented that help distinguish between the three different regimes.

Barad & Fringer (2010) and Troy & Koseff (2005) both predicted that ISWs and progressive interfacial wave trains respectively, will develop instabilities when the growth rate of an unstable mode (corresponding to a locally parallel flow) exceeds a critical value of $\bar{\sigma}_i T_w = 5$, where $\bar{\sigma}_i$ is the growth rate of the instability averaged over T_w, the period in which parcels of fluid are subjected to $Ri < 1/4$. Barad & Fringer (2010) suggested that a critical bound of $\bar{\sigma}_i T_w = 1$ can be inferred for the data presented in Fructus *et al.* (2009). They hypothesized that the smaller threshold in Fructus *et al.* (2009) may be due to disturbances present in the laboratory. A linear stability analysis is presented here which shows that the growth rate of an instability is very sensitive to the amplitude of the wave, the ratio of the undisturbed layer depths and the sharpness of the pycnocline (the smoothing distance over which transition from one layer to another is made in the background stratification). Barad & Fringer (2010) did not take account of variations in the sharpness of the pycnocline or in the depths of the upper and lower layers. Hence the difference in the critical $\bar{\sigma}_i T_w$ is conjectured to be due to differences in the undisturbed density field rather than disturbances in the laboratory. A more thorough discussion of this is given in §5.

The paper is outlined as follows. The governing equations are presented in §2 and a summary of their numerical solution is given in §3. In §4, the waves are classified and stability curves are presented. In §5, results from a linear stability analysis are given and finally in §6 a short summary of the main findings are given along with a discussion of current field observations.

2. Governing Equations

To model the time dependent motion of an ISW, the inviscid, incompressible, Oberbeck-Boussinesq equations in two dimensions may be used:

$$\rho_0 \left(\mathbf{u}_t + \mathbf{u} \cdot \nabla \mathbf{u}\right) = -\nabla p - \rho g \mathbf{j}, \tag{2.1}$$

$$\rho_t + \mathbf{u} \cdot \nabla \rho = 0, \tag{2.2}$$

$$\nabla \cdot \mathbf{u} = 0, \tag{2.3}$$

where ρ_0 is a convenient constant reference density, $\mathbf{u} = (u, v)$ is the fluid velocity vector, t denotes time, $\nabla = (\partial/\partial x, \partial/\partial y)$ is the gradient operator, p is the fluid pressure, ρ is the fluid density, g is the acceleration due to gravity and $\mathbf{j}$ is the unit vector in the vertical direction. Note that the Boussinesq approximation is routinely used and accepted in the literature when studying oceanic ISWs. However, Long (1965) and Benjamin (1966) showed that finite amplitude internal waves may depend crucially on small effects neglected in the Boussinesq approximation. In particular, they call for care when using the approximation if quantities other than the non-dimensional density difference are small. A thorough investigation of the non-Boussinesq regime, in the context presented here, is currently in progress but beyond the scope of the present paper. Buoyancy and vorticity are introduced as $b = -g(\rho - \rho_0)/\rho_0$ and $\zeta = v_x - u_y$, respectively. Then taking the curl of the momentum equation (2.1) and rewriting (2.1) and (2.2) in terms of vorticity and buoyancy gives

$$\zeta_t + \mathbf{u} \cdot \nabla \zeta = b_x, \tag{2.4}$$

$$b_t + \mathbf{u} \cdot \nabla b = 0, \tag{2.5}$$

$$\nabla \cdot \mathbf{u} = 0. \tag{2.6}$$

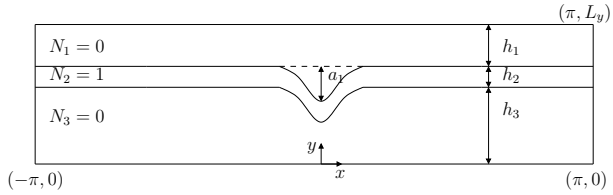

FIGURE 1. A schematic diagram of the computational domain.

To study the evolution of an ISW satisfying (2.4)-(2.6) two numerical schemes are employed. The first, which is outlined in detail in King *et al.* (2010) and briefly in §3.2, is an iterative procedure which finds a steady state solution. The second, which is outlined in detail in Dritschel & Fontane (2010) and briefly in §3.3, is the Combined Lagrangian Advection Method (CLAM) which takes a steady state solution as input and evolves it with time.

3. Numerical Method

3.1. *Numerical Setup*

A computational domain is set up that is 2π periodic in the horizontal x direction and bounded above and below by rigid boundaries at $y = 0$ and $y = L_y$, see figure 1. The aspect ratio of the domain, $L_y/2\pi$, is chosen to be 0.05 throughout the paper. This ensures that the domain is long compared to the length of the waves. A three layer stratification is considered in which a linearly stratified middle layer is sandwiched between homogeneous layers. The thicknesses of the top, middle and bottom layers are denoted by h_1, h_2 and h_3 respectively. The domain is chosen so that the ISW is located in the centre of the domain as shown. The maximum displacement of the interface between the top and middle layers is denoted by a_1. The undisturbed Brunt-Väisälä frequency, N, is defined by

$$N^2(Y) = \frac{\mathrm{d}\bar{b}}{\mathrm{d}Y} = -\frac{g}{\rho_0}\frac{\mathrm{d}\bar{\rho}}{\mathrm{d}Y},$$

where Y is an isopycnal coordinate used to denote y in the far field and bars denote background (undisturbed) variables. The undisturbed Brunt-Väisälä frequency is assumed to be zero in the top and bottom layers, unity in the middle layer, and to have a smooth transition between these values such that

$$N^2(Y) = \frac{1}{2}\mathrm{erf}\left(\frac{Y-h_3}{\delta}\right) - \frac{1}{2}\mathrm{erf}\left(\frac{Y-(h_2+h_3)}{\delta}\right),$$

where erf denotes the error function and δ represents a distance over which the profile is smoothed. A value of two y grid lengths is chosen for δ unless stated otherwise. A discussion of this choice and the effect of varying δ is given in King *et al.* (2010) and in §5. Unless stated otherwise, a resolution of $(n_x, n_y) = (1024, 128)$, where n_x and n_y are the number of grid points in the horizontal and vertical directions respectively, is used throughout. Justification for this choice of resolution is given in §5.

3.2. *The steady state solver*

To find a steady state solution the numerical scheme of King *et al.* (2010) is utilized. Following Yih (1960) and Grue *et al.* (2000) it was shown in King *et al.* (2010) that (2.1) (or equivalently (2.4)) can be rewritten as

$$\zeta = \nabla^2\psi = -\frac{N^2(Y)}{c^2}\psi, \tag{3.1}$$

where $\psi(x, y)$ is the streamfunction, defined such that $v = \psi_x$, and $u = -\psi_y$. Solutions of (3.1) for a given $N^2(Y)$ are computed using an iterative procedure. First, a uniform computational grid is set up within the domain. The background buoyancy field, $\bar{b}(Y)$, is then found by integrating a given profile of $N^2(Y)$ with respect to Y. The iterative solution procedure is then started with a guess for ψ. A weakly nonlinear solitary wave solution is used for this purpose which is known to be accurate at small wave amplitudes. The wave amplitude is defined as $\mathcal{A} = \eta_{rms} = \psi_{rms}/c$, where η is the (downward) streamline displacement and *r.m.s* denotes the root-mean-square value. By using the

wave speed c_{wnl} from the weakly nonlinear solution, an initial amplitude $\mathcal{A}_0 = \psi_{rms}/c_{wnl}$ is found. This initial guess is then corrected by solving

$$Y = y + \frac{\psi(x,y)}{c}, \tag{3.2}$$

for the isopycnal coordinate Y followed by (3.1) for ζ at each point in the domain (using the previous guess for ψ in the right hand side of (3.1)). Spectral inversion of $\nabla^2\psi = \zeta$ provides an updated value for ψ, and

$$c = \frac{\psi_{rms}}{\mathcal{A}}, \tag{3.3}$$

provides an updated value for c. This process is then repeated, by solving (3.2), (3.1), and (3.3) until ψ converges. Subsequent states are found for higher amplitudes by increasing $\mathcal{A}$ in increments of $\delta\mathcal{A} = 0.001$.

3.3. *The unsteady solver*

To study the evolution of a steady state satisfying (2.4)-(2.6) the numerical procedure outlined in Dritschel & Fontane (2010) is utilized. Note that no perturbations (or noise) are added to the steady state. A hyperdiffusive vorticity term $\nu_6\nabla^6\zeta$ (with diffusion coefficient $\nu_6 = 2^{-54}$) is added to the right hand side of (2.4) in order to stabilize the solution. The unsteady simulations are then carried out using CLAM, a combination of contour advection (Dritschel & Ambaum 1997) and pseudo-spectral techniques in order to integrate (2.5) forward in time. This provides an accurate source term for the right hand side of (2.4), which is solved using a pseudo-spectral method. Temporal integration is performed using a fourth order Runge-Kutta integration scheme. Further details of the method can be found in Dritschel & Fontane (2010).

4. Numerical Results

The numerical model is tested over a parameter range in which the undisturbed background stratification is varied via the parameters $h_2/(h_1+h_2) \in [0.10, 0.91]$ and $h_3/(h_1+h_2) \in [2.33, 11.5]$. As previously noted, the aspect ratio of the computational domain, $L_y/2\pi = 0.05$, is fixed throughout and unless stated otherwise a resolution of $(n_x, n_y) = (1024, 128)$ is utilized. In addition, the distance, δ, over which the undisturbed Brunt-Väisälä frequency profile is smoothed is set at two y grid lengths, ($2L_y/n_y = 0.0049$) (unless given otherwise). Hence the minimum value of h_2 that can be investigated is restricted by the fact that the middle layer must be at least two y grid lengths thick which in turn is restricted by the resolution considered. Similarly the minimum value of h_1 that can be investigated, (or equivalently the maximum value of $h_2 + h_3$ since $h_1 + h_2 + h_3 = L_y$) is limited by the fact that the top layer must be at least two y grid lengths thick to allow for smoothing into the top layer. Attention is restricted to modelling ISWs of depression, i.e. $h_3 > (h_1 + h_2)$. Waves of elevation can be obtained by symmetry for $h_3 < (h_1 + h_2)$. In order to compare with previous works, in particular Fructus *et al.* (2009) and Barad & Fringer (2010), a subset of the parameter space, namely $h_2/(h_1+h_2) \in [0.13, 0.80]$ and $h_3/(h_1+h_2) \in [3.35, 5.67]$ is focused upon here. Unless stated otherwise, the computations are performed in a frame of reference moving at the wave speed c and all results are presented in this frame of reference.

4.1. *Classification of Breaking*

The waves are classified into three different types: stable, weakly unstable and unstable. This is achieved by (i) calculating the percentage increase in several parameters in the numerical system over 100 time units (approximately 16 buoyancy periods based on the maximum N or around 50 rotation periods based on the maximum initial $|\zeta|$) and analyzing the variation in the percentage increase in these parameters with increments

in wave amplitude, and (ii) a visual inspection of the numerical evolution of the vorticity and buoyancy fields over 100 time units. A simulation duration of 100 time units is chosen for the classification process as typically the classification state (stable, weakly unstable, unstable) of an observed wave over 100 time units tended to remain the same over larger simulation durations ($t = 200$) but varied over shorter computations ($t = 50$). In table 1, by way of illustration, the percentage increase in the parameters found most useful in helping to classify stability with an increase in the non-dimensional amplitude are given when $h_2/(h_1 + h_2) = 0.13$ and $h_3/(h_1 + h_2) = 3.35$. Enstrophy and palenstrophy are defined as, $\mathcal{E} = \int_{\mathcal{D}} |\zeta|^2 dxdy$ and $\mathcal{P} = \int_{\mathcal{D}} |\nabla\zeta|^2 dxdy$, respectively, where $\mathcal{D}$ is the two dimensional computational domain, $|\zeta|_{max}$ is the maximum vorticity in $\mathcal{D}$, ζ_{rms} is the root mean square of the vorticity field in $\mathcal{D}$, $s(c_{b,t,m})$, are the arc lengths of an isopycnal situated at the bottom, top or middle of the pycnocline respectively, $|\nabla b|_{max}$ is the maximum of the gradient of the buoyancy in $\mathcal{D}$ and ∇b_{rms} is the root mean square of the gradient of the buoyancy field in $\mathcal{D}$. The percentage increase in available potential energy, kinetic energy, circulation and the mean square displacement of a given isopycnal from the isopycnal mean height tracing the top, the middle or the bottom, of the pycnocline respectively were all investigated for different wave types but did not show any significant differences over 100 time units and so could not be used to help classify stability.

It can be seen from table 1 that as the amplitude of the wave increases (for a given undisturbed background stratification) the percentage increase in the parameters considered tends to increase as well (though the increase is not always monotonic in all parameters). To classify a change in the stability state of a given wave a marked increase (or decrease) in the percentage increase of one or all of the parameters considered is required. For example in table 1, all waves that are classified as stable have similar percentage changes in all parameters considered and the percentages are of a small value.

$\frac{a_1}{h_1+h_2}$	$\mathcal{E}$	$\log_{10}(\mathcal{P})$	$\lvert\zeta\rvert_{max}$	ζ_{rms}	$s(c_b)$	$s(c_t)$	$s(c_m)$	$\lvert\nabla b\rvert_{max}$	∇b_{rms}	Classification
0.853	**0.157**	**0.891**	**0.780**	**0.078**	**0.103**	**0.091**	**0.001**	**0.114**	**-0.022**	**Stable**
0.909	0.158	0.806	1.105	0.079	0.007	0.023	0.001	0.292	-0.020	Stable
0.960	0.153	0.742	1.616	0.076	0.031	0.024	0.002	0.546	-0.022	Stable
1.006	0.192	0.820	1.556	0.096	0.109	0.011	0.002	0.329	-0.024	Stable
1.048	0.292	0.979	2.690	0.146	0.049	0.034	0.004	0.529	-0.021	Very weak
1.084	**1.109**	**3.640**	**0.752**	**0.553**	**0.066**	**0.022**	**0.321**	**5.824**	**0.035**	**Weak**
1.116	5.383	11.099	3.069	2.656	0.143	0.869	5.350	39.277	0.826	Unstable
1.143	**20.170**	**22.687**	**3.808**	**9.622**	**3.958**	**11.078**	**18.271**	**96.067**	**3.211**	**Unstable**

TABLE 1. Percentage increase (or decrease if negative number) in a given parameter: $\mathcal{E}$, $\log_{10}(\mathcal{P})$, $|\zeta|_{max}$, ζ_{rms}, $s(c_b)$, $s(c_t)$, $s(c_m)$, $|\nabla b|_{max}$, ∇b_{rms} for a wave of amplitude $a_1/(h_1+h_2)$ with undisturbed background layer thicknesses $h_2/(h_1+h_2) = 0.13$ and $h_3/(h_1+h_2) = 3.35$.

A marked increase in the percentage increases is seen in the weak case compared with the stable cases and a further jump in the percentage increases is seen in the unstable cases. In general, it is not possible to use one percentage increase in a single parameter to consistently make a distinction between stability states and in addition the amount by which the percentage increases changes from state to state varies for different background stratification. Typically, identification of the boundary between unstable and weakly unstable waves is easier to establish than the bound between weakly unstable and stable waves, as a marked difference in percentage increases in one or more parameters between these states is easier to identify. To establish the boundary between unstable and weakly unstable states a visual inspection of the buoyancy field and vorticity fields is used in addition to the numerical values investigated.

As an example, evolutions of the vorticity field ζ and the buoyancy field b in stable, weakly unstable and unstable waves are presented in figures 2 to 7, respectively. In all six figures the wave propagates from left to right. Successive plots are at times $t = 0, 25, 50, 75$ and 100 with time increasing downwards. The three waves depicted in figures 2-7 are highlighted in bold in table 1. Waves that are classified as stable show little or no change in form as they evolve (see figures 2 and 3) and the percentage increase in the various theoretical parameters associated with the wave are very small (see table 1). Waves which are classified as weakly unstable exhibit a small deformation of the interface and either no coherent billows are formed or they quickly collapse again (see the lower three panels of figures 4 and 5), and the percentage increases studied are small but in general bigger than in the stable cases (see table 1). Waves which are classified as unstable exhibit persistent coherent billows on the interface (see the lower three panels of figures 6 and 7) and the percentage increase in the parameters discussed in table 1 are significantly bigger than in the weakly unstable and stable cases respectively.

The instability seen in figures 6 and 7 is typical of what is seen in all waves which are classified as unstable throughout the paper. It takes the form of Kelvin-Helmholtz billows forming on the pycnocline. The instability is not a numerical artifact, it is a physical response to the strong shear force exerted across the pycnocline. This has been seen previously in ISWs of this type in (a) the field (Moum *et al.* 2003), (b) the laboratory (Fructus *et al.* 2009) and in (c) numerical simulations (Barad & Fringer 2010). A comparison of the findings made here with those presented in Moum *et al.* (2003), Fructus *et al.* (2009) and Barad & Fringer (2010) will be made later in the paper. Note that in waves classified as weakly unstable, oscillations of the isopycnals occur but the instabilities do not have sufficient time to grow into persistent coherent billows.

Figures 8 (a), (b) and (c) show the sensitivity of stable, weakly unstable and unstable

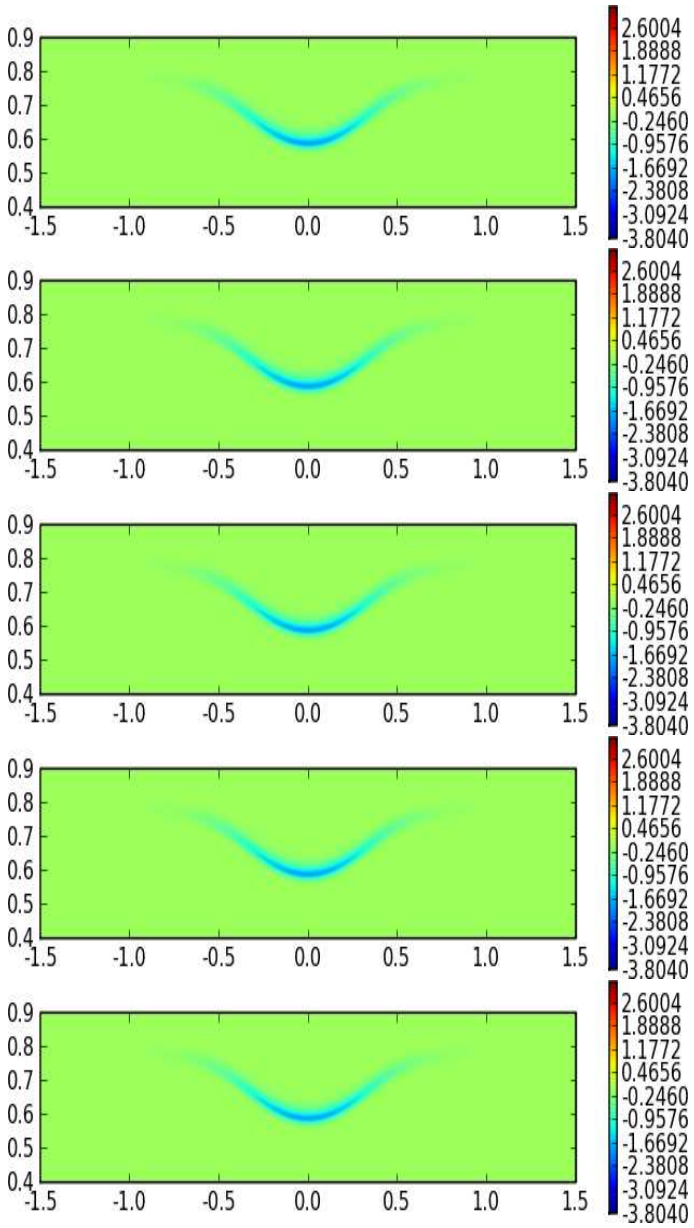

FIGURE 2. Sequence showing the evolution of the vorticity field, ζ, for an ISW with, $a_1/(h_1+h_2) = 0.853$, $h_2/(h_1+h_2) = 0.13$ and $h_3/(h_1+h_2) = 3.35$. Successive plots are at times $t = 0, 25, 50, 75, 100$ with time increasing downwards. $(x, y/L_y) \in [-1.5, 1.5] \times [0.4, 0.9]$. This wave is classified as stable. See complementary online movie 1.

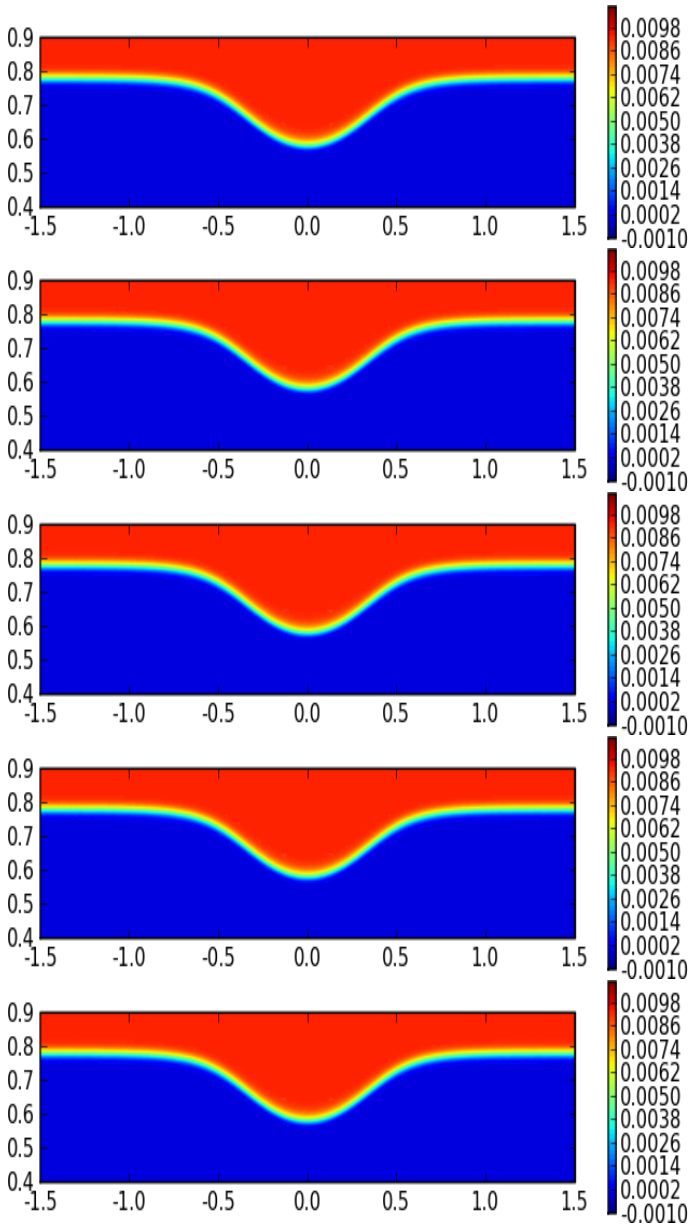

FIGURE 3. Sequence showing the evolution of the buoyancy field, b, corresponding to the same ISW as in figure 2. See complementary online movie 2.

simulations respectively, to the resolution of the computations (and the number of contours utilized in CLAM). The three different waves in figures 8 (a), (b) and (c) correspond to the three waves presented in figures 3, 5 and 7 respectively. The average normalized

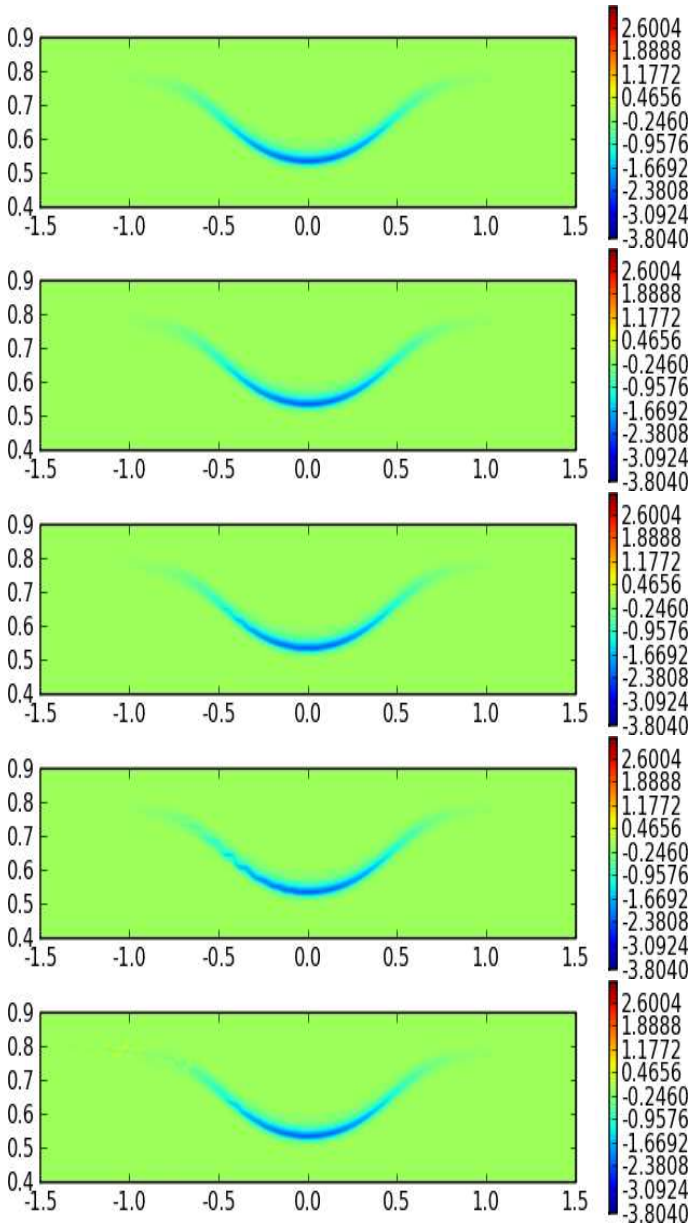

FIGURE 4. Sequence showing the evolution of the vorticity field, ζ, for an ISW with, $a_1/(h_1 + h_2) = 1.084$. All other variables are the same as in figure 2. This wave is classified as weakly unstable. See complementary online movie 3.

absolute error in the buoyancy field (for a given wave) $\overline{|b - b^*|}/|b^*|_{max}$, is plotted against simulation time t, where b^* is the buoyancy field in an equivalent simulation computed at a resolution of $(n_x, n_y) = (2048, 256)$ utilizing ten times as many contours (800) than

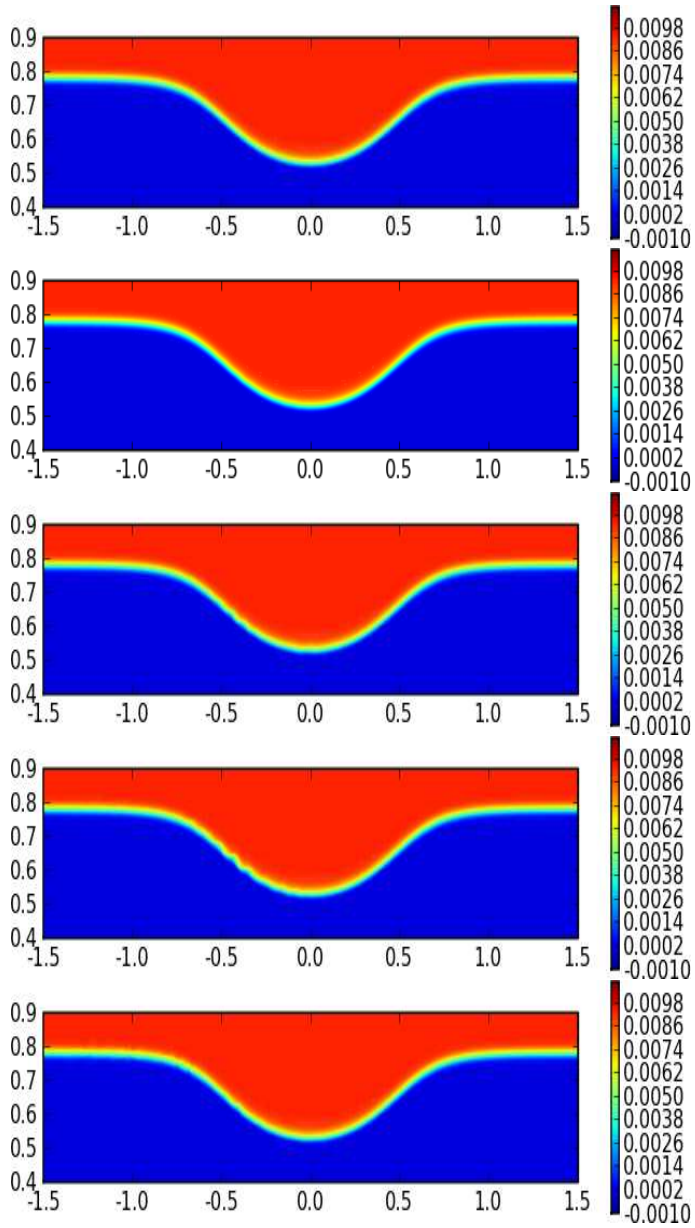

FIGURE 5. Sequence showing the evolution of the buoyancy field, b, corresponding to the same ISW as in figure 4. See complementary online movie 4.

in the standard simulations (80) presented throughout this paper. Figure 8 shows that (i) there is very little difference between resolutions of $(n_x, n_y) = (1024, 128)$ ($\triangledown$) and $(n_x, n_y) = (2048, 256)$ ($\triangle$), and that (ii) there is little difference between using 80 con-

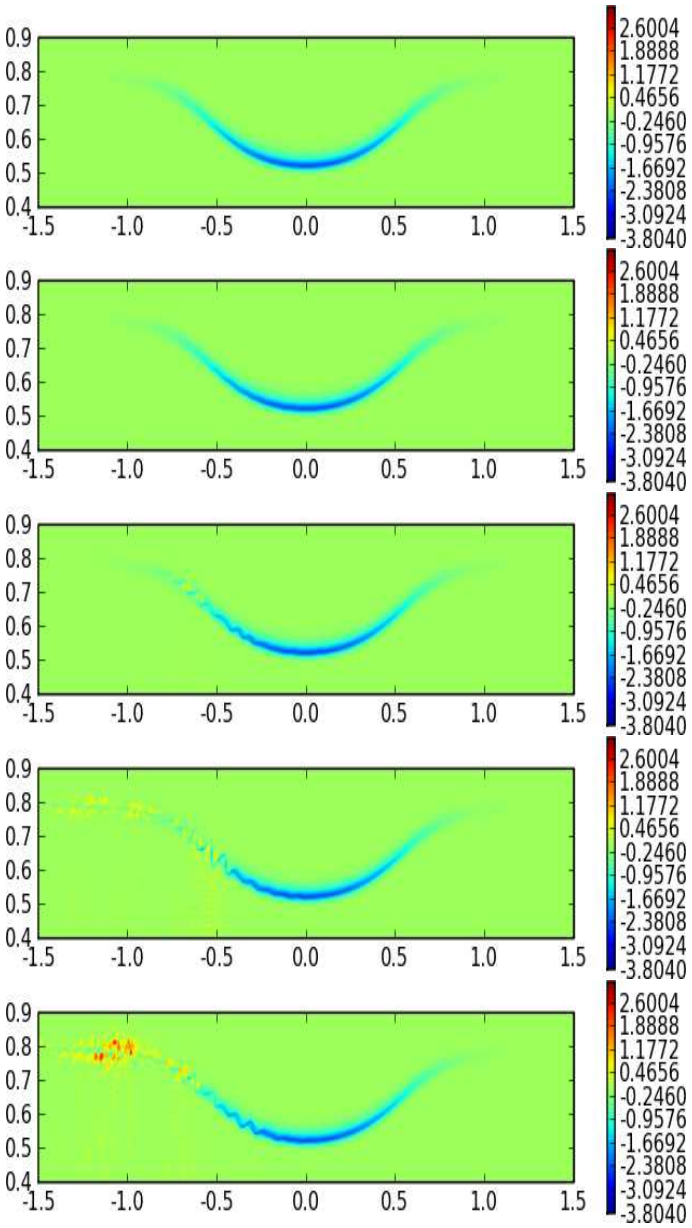

FIGURE 6. Sequence showing the evolution of the vorticity field, ζ, for an ISW with, $a_1/(h_1 + h_2) = 1.143$. All other variables are the same as in figure 2. This wave is classified as unstable. See complementary online movie 5.

tours in CLAM (in this context) as opposed to 800. Hence throughout this paper, the unsteady numerical computations use a resolution of $(n_x, n_y) = (1024, 128)$ and employ

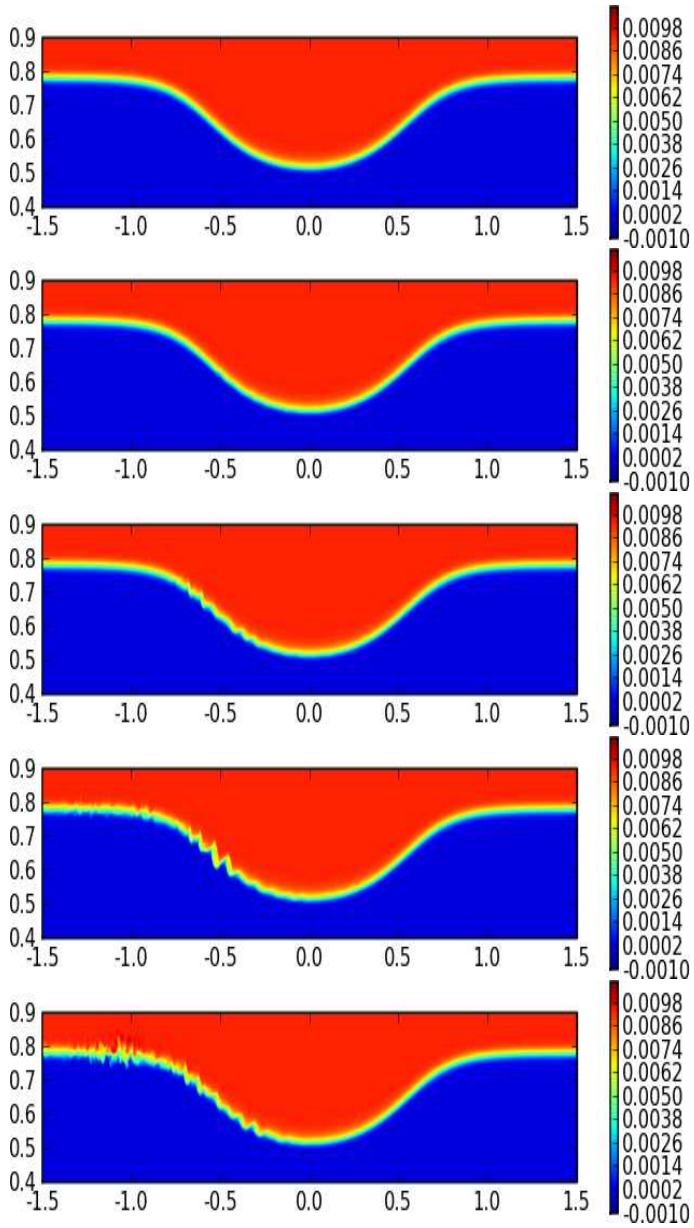

FIGURE 7. Sequence showing the evolution of the buoyancy field, b, corresponding to the same ISW as in figure 6. See complementary online movie 6.

80 contours. Note that the average normalized absolute error in the vorticity field shows a similar trend to that of the buoyancy field.

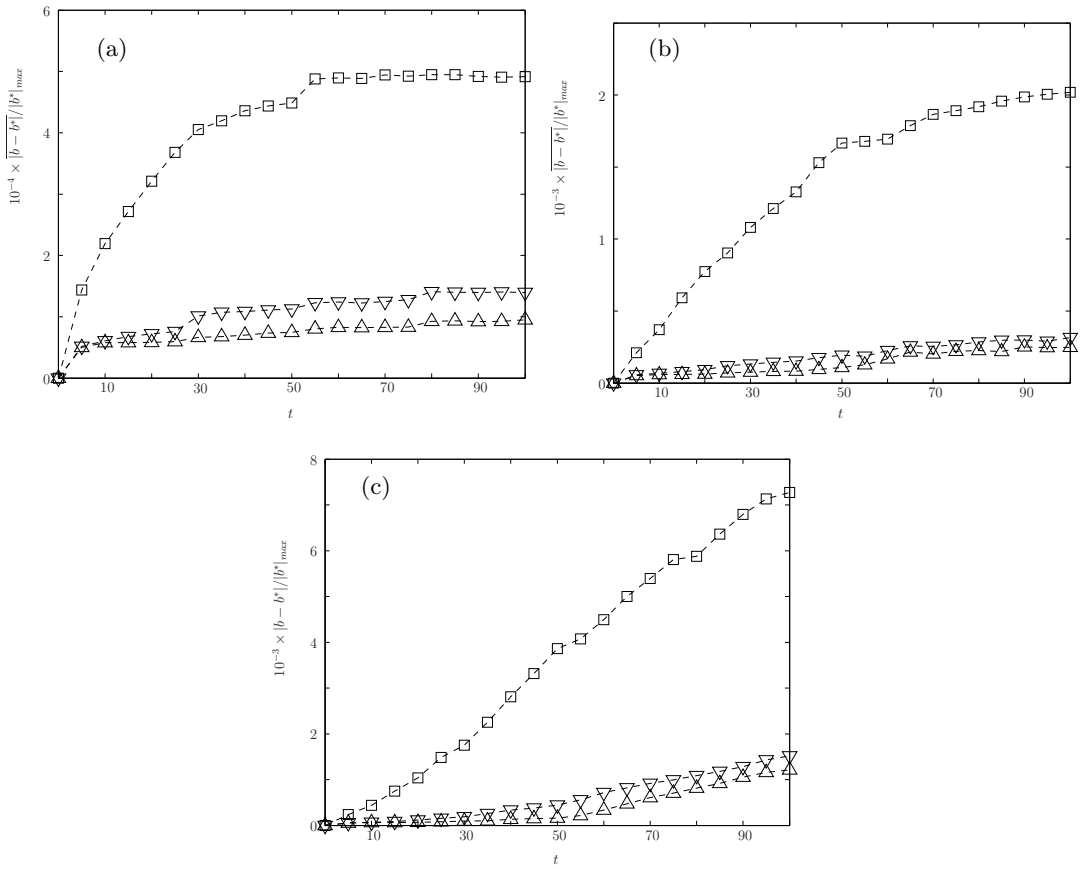

FIGURE 8. The average normalized abolute error in the buoyancy field $10^{-4} \times \overline{|b-b^*|}/|b^*|_{max}$ versus simulation time t. (a) $a_1/(h_1+h_2) = 0.853$, (b) $a_1/(h_1+h_2) = 1.084$ and (c) $a_1/(h_1+h_2) = 1.143$. The wave in (a) is classified as stable and the corresponding evolution of b is given in figure 3. The wave in (b) is classified as weakly unstable and the corresponding evolution of b is given in figure 5. The wave in (c) is classified as unstable and the corresponding evolution of b is given in figure 7. $h_2/(h_1+h_2) = 0.13$ and $h_3/(h_1+h_2) = 3.35$. $(n_x, n_y) = (512, 64)$ ($\square$), $(n_x, n_y) = (1024, 128)$ ($\triangledown$), $(n_x, n_y) = (2048, 256)$ ($\triangle$).

4.2. *Stability Curves*

For all waves investigated, stability curves can be obtained by identifying the largest amplitude stable state and the smallest amplitude unstable state. In figure 9, stability curves are presented for the non-dimensional amplitude, $a_1/(h_1+h_2)$, versus the non-

dimensional pycnocline thickness, $h_2/(h_1+h_2)$, for three data sets in which the non-dimensional lower layer thickness $h_3/(h_1+h_2) = 3.35$ ($\diamond$), 4 ($*$), 5.67 ($\times$) varies. Symbols joined by a solid/dashed line denote stable/unstable observations respectively. The area in between the solid and dashed curves marks a weakly unstable region for a given data set. It is clear from figure 9 that the critical amplitude required for instability increases with increases in both $h_2/(h_1+h_2)$ and $h_3/(h_1+h_2)$. In other words, an increase in $h_2/(h_1+h_2)$ or $h_3/(h_1+h_2)$ stabilizes the system. This is expected for $h_2/(h_1+h_2)$ since the thicker the pycnocline is, the weaker the shear across it will be, and hence the larger will be the amplitude required to excite instability. Note that when $h_3/(h_1+h_2) = 3.35$ ($\diamond$) and $h_2/(h_1+h_2) \gtrapprox 0.4$ no unstable waves are observed and hence no bound between unstable and weakly unstable waves can be established. Weakly unstable waves are observed, hence, a bound between weakly unstable and stable waves can be found but for clarity is not displayed. Similarly for $h_3/(h_1+h_2) = 2.33$ and $h_2/(h_1+h_2) \in [0.100, 0.167]$ (data not displayed) a bound between weakly unstable waves and stable waves can be established but no unstable waves are observed and moreover for $h_2/(h_1+h_2) > 0.167$ all waves computed are stable (no weakly unstable or unstable waves are observed). In addition, the three stability curves in figure 9 show that the region of weak instability decreases in width as $h_2/(h_1+h_2)$ increases. This suggests that once the stability (solid) and instability (dashed) curves converge the system cannot support unstable waves (weakly unstable waves may still form though) and in particular, for fixed values of $h_3/(h_1+h_2)$, if $h_2/(h_1+h_2)$ is sufficiently large, unstable waves cannot exist. As it is not possible to compute at higher values of $h_2/(h_1+h_2)$ than in figure 9 (they are restricted by the computational domain height $L_y = h_1+h_2+h_3$) it is not possible to confirm the conjecture above.

Figure 10 shows the same data set as in figure 9 but plots against $\mathcal{A}$ as opposed to

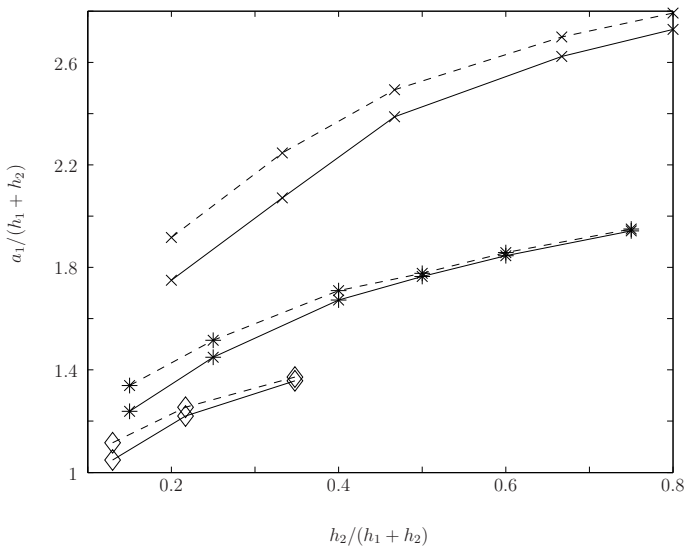

FIGURE 9. Stability diagram for different values of the lower layer thickness, $h_3/(h_1+h_2) = 3.35$ ($\diamond$), 4 ($*$), 5.67 ($\times$). Non-dimensional amplitude, $a_1/(h_1+h_2)$, versus non-dimensional pycnocline thickness, $h_2/(h_1+h_2)$. Symbols joined by a solid/dashed line denote stable/unstable observations respectively.

$a_1/(h_1+h_2)$. Note that figure 10 does not exhibit the same trend as in figure 9 of the stability and instability curves converging for large values of $h_2/(h_1+h_2)$. Recall that $\mathcal{A} = \psi_{rms}/c$ and the increment in amplitude in the numerical simulations is fixed at $\delta\mathcal{A} = 0.001$ (see §3.2). The increment in $a_1/(h_1+h_2)$, therefore, investigated in figure 9 is variable and may offer an alternative explanation as to why the width of the weakly unstable region varies with $h_2/(h_1+h_2)$.

In Fructus *et al.* (2009), experimental observations of stable and unstable waves were made and it was reported that breaking waves occurred for amplitudes above a critical threshold of $a_1 = 2.24\sqrt{h_1h_2}(1+h_2/h_1)$ when $h_2/h_1 < 1$. To compare their data with the numerical findings presented here a plot of $a_1/\sqrt{h_1h_2}(1+h_2/h_1)$ versus h_2/h_1 is given in figure 16 for the same data set as that presented in figures 9 and 10. The row of horizontal black dots marks the critical amplitude predicted by Fructus *et al.* (2009). In

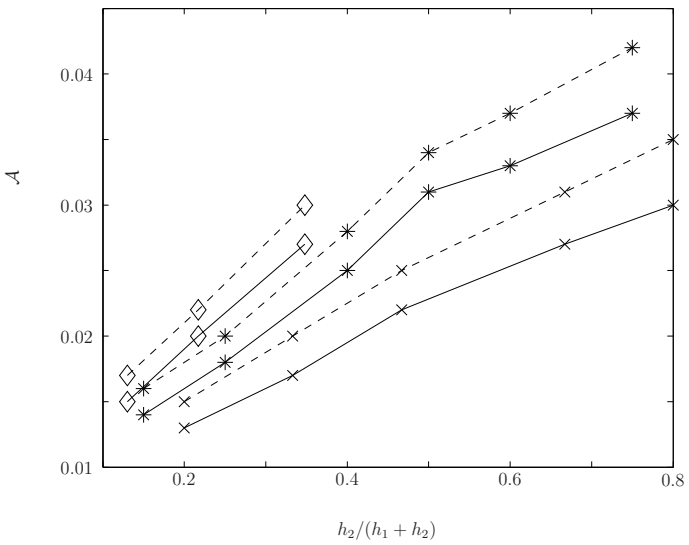

FIGURE 10. Stability diagram for different values of the lower layer thickness, $h_3/(h_1+h_2) = 3.35$ ($\diamond$), 4 ($*$), 5.67 ($\times$). Wave amplitude, $\mathcal{A}$, versus non-dimensional pycnocline thickness, $h_2/(h_1+h_2)$. Symbols joined by a solid/dashed line denote stable/unstable observations respectively.

Fructus *et al.* (2009), $h_3/(h_1+h_2)$ varied between 3.22 and 7.25 but no account of this variation was made. The numerical results in figure 16 show that the critical amplitude marking the threshold between stability and instability is dependent on both h_2/h_1 and $h_3/(h_1+h_2)$, and hence the bound given in Fructus *et al.* (2009) is not general. The shape of the stability curves presented in figure 16 are in good agreement with the fully nonlinear solutions presented in figure 2 of Fructus *et al.* (2009). The fully nonlinear solution presented in Fructus *et al.* (2009) was calculated at $h_3/(h_1+h_2) = 4.13$ and $Ri = 1/4$. The stability bounds presented in figure 16 suggest a stability curve for $h_3/(h_1+h_2) = 4.13$ at a slightly higher amplitude than the fully nonlinear curve in Fructus *et al.* (2009). This is to be expected since Fructus *et al.* (2009) show that a Ri number somewhat smaller than 1/4 is required for instability and hence their fully

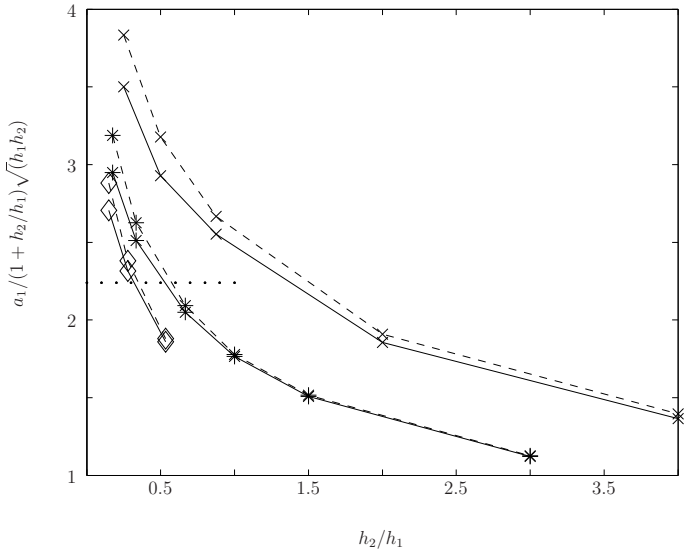

FIGURE 11. Stability diagram for different values of the lower layer thickness, $h_3/(h_1+h_2) = 3.35$ ($\diamond$), 4 ($*$), 5.67 ($\times$). Non-dimensional amplitude, $a_1/\sqrt{h_1h_2}(1+h_2/h_1)$, versus non-dimensional pycnocline thickness, h_2/h_1. Symbols joined by a solid/dashed line denote stable/unstable observations respectively. The horizontal line of black dots correspond to the bound reported in Fructus *et al.* (2009).

nonlinear solution (which is computed at $Ri = 1/4$) is expected to underpredict the amplitude required for instability.

In figure 12, stability curves are presented for the minimum Richardson number Ri_{min} versus the non-dimensional pycnocline thickness $h_2/(h_1+h_2)$ for the same data set as that presented in figures 9 to 16. The Richardson number represents a balance between the destabilizing effects of velocity shear through ζ^2 and the stabilizing effects of stratified buoyancy through b_y. Hence as the thickness of the pycnocline, $h_2/(h_1+h_2)$ increases the critical minimum Richardson number required for instability is expected to decrease. However, there is no clear trend of this form in figure 12. Hence, Ri_{min} may not be the best parameter to use when assessing stability. This has been noted previously by Troy & Koseff (2005) who studied long internal wave trains and by Fructus *et al.* (2009)

who studied ISWs. However, motivated by the fact that the Richardson number is easily computed from field observations, researchers continue to seek a global Ri_{min} to assess stability. Barad & Fringer (2010) have recently presented numerical results which suggest that a minimum Richardson number of 0.1 ± 0.01 is required for instability in ISWs. Note that the undisturbed stratification in Barad & Fringer (2010) is defined such that H_1 denotes the upper layer thickness, H_2 is the lower layer thickness and the total depth of the fluid is $H_1 + H_2$. Their pycnocline has a thickness of δ_0 and is situated such that the mid-depth of the pycnocline is at the interface between the upper and lower layers. The stratification in Barad & Fringer (2010) can be approximated here by setting $h_1 = H_1 - \delta_0/2, h_2 = \delta_0$, and $h_3 = H_2 - \delta_0/2$. Barad & Fringer (2010) computed their bound via twelve simulations over a parameter range, which in the notation used here, encompasses $h_2/(h_1 + h_2) \in [0.049, 0.571]$ and $h_3/(h_1 + h_2) \in [2.571, 3.878]$. The global lower bound for instability suggested by Barad & Fringer (2010) of 0.1 ± 0.01 for ISWs is in good agreement with the data set shown in figure 12, in the sense that $Ri_{min} = 0.1$ provides a lower bound for instability for the data set presented in figure 12. However, figure 12 shows that the critical Ri_{min} is a function of $h_3/(h_1 + h_2)$ and $h_2/(h_1 + h_2)$. Hence a much sharper bound than the global bound suggested by Barad & Fringer (2010) can be ascertained for the critical Ri_{min} if $h_3/(h_1 + h_2)$ and $h_2/(h_1 + h_2)$ are known.

Moreover, figure 12 suggests that higher values of $h_3/(h_1 + h_2)$ may exhibit values of Ri_{min} that are smaller than the global bound suggested by Barad & Fringer (2010). In figure 13, the critical Richardson number required for instability Ri_{crit} versus the non-dimensional lower layer depth $h_3/(h_1 + h_2)$ is plotted for an extended data set which includes $h_3/(h_1 + h_2) = 9$ and 11.5. For $h_3/(h_1 + h_2) = 3.35, 4$, and 5.67, Ri_{crit} was calculated by taking the average value of Ri_{min} for the unstable bounds (dashed lines) presented in figure 12. The variance in the data about the average is marked by error bars

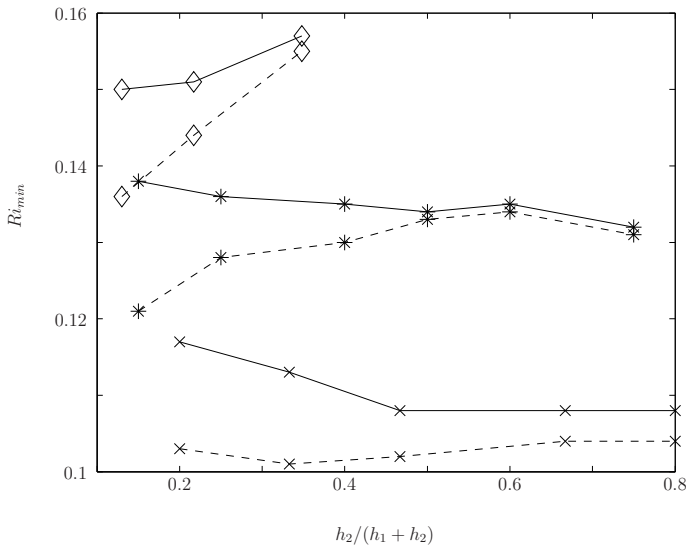

FIGURE 12. Stability diagram for different values of the lower layer thickness, $h_3/(h_1+h_2) = 3.35$ ($\diamond$), 4 ($*$), 5.67 ($\times$). Minimum Richardson number Ri_{min} versus non-dimensional pycnocline thickness $h_2/(h_1+h_2)$. Symbols joined by a solid/dashed line denote stable/unstable observations respectively.

in figure 13. This procedure was repeated for $h_3/(h_1+h_2) = 9$ for six data points over a range, $h_2/(h_1+h_2) \in [0.2, 0.7]$. When $h_3/(h_1+h_2) = 11.5$, the pycnocline approaches the upper boundary of the domain, and it is only possible to compute over a limited range of $h_2/(h_1+h_2) \in [0.25, 0.30]$. Three data points are computed for $h_3/(h_1+h_2) = 11.5$ at $h_2/(h_1+h_2) = 0.25, 0.275$ and 0.30. The data in figure 13 clearly show that Ri_{crit} varies with $h_3/(h_1+h_2)$. Moreover, critical values of Ri can be found that are below the global minimum suggested by Barad & Fringer (2010), namely 0.1 ± 0.01, if $h_3/(h_1+h_2)$ is sufficiently large.

Fructus *et al.* (2009) suggested that a sharper bound than Ri_{min} for assessing the stability of ISWs may be the parameter L_x/λ, where L_x is the width of the region in the pycnocline in which $Ri \leqslant 1/4$ and λ is the half width of the wave. They found breaking waves occurred when $L_x/\lambda \geqslant 0.86$ and that the waves were stable otherwise. In figure 14,

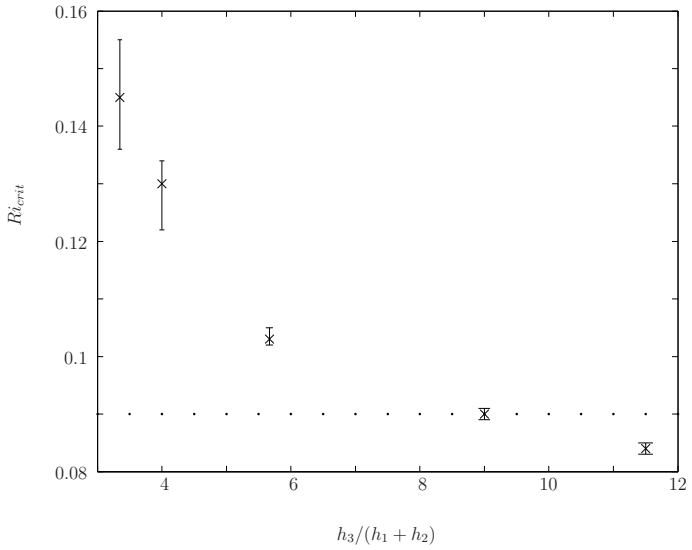

FIGURE 13. Critical Richardson number Ri_{crit} versus non-dimensional lower layer thickness $h_3/(h_1+h_2)$. Crosses denote unstable observations and straight lines are error bars. The horizontal dotted line at $Ri_{crit} = 0.9$ represents the global bound suggested by Barad & Fringer (2010).

stability curves are presented for L_x/λ versus the non-dimensional pycnocline thickness $h_2/(h_1+h_2)$ for the same three data sets as presented in figures 9 to 12. It can be seen from figure 14 that L_x/λ clearly varies with $h_2/(h_1+h_2)$ and $h_3/(h_1+h_2)$. Fructus *et al.* (2009) found the bound $L_x/\lambda \geqslant 0.86$ despite variations in $h_3/(h_1+h_2)$ and $h_2/(h_1+h_2)$. Their stability bound is for $3.22 < h_3/(h_1+h_2) < 7.14$ and $0.27 < h_2/(h_1+h_2) < 0.79$, and should therefore be used with caution.

5. Linear Stability Analysis

To determine the growth rate and propagation speed of the unstable modes seen in the numerical simulations, a stability analysis that solves the Taylor-Goldstein equation (Hazel 1972, see (1.1)) is performed. It is assumed that when the wave is at maximum displacement, a vertical section through the flow behaves as parallel shear flow. The

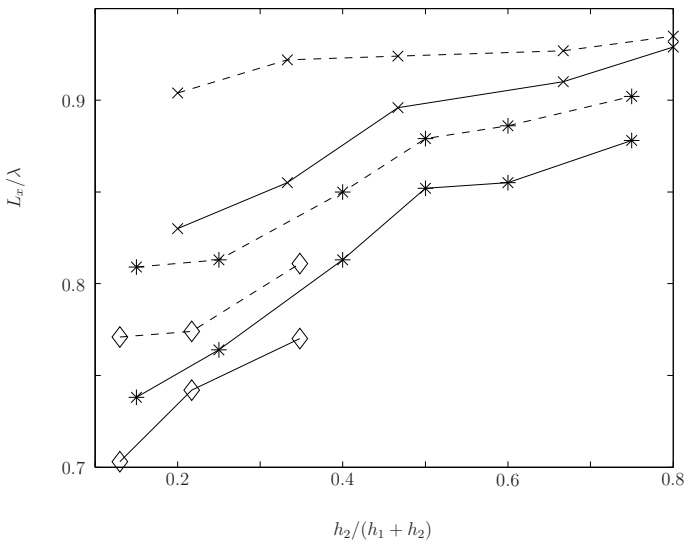

FIGURE 14. Stability diagram for different values of the lower layer thickness, $h_3/(h_1+h_2) = 3.35$ ($\diamond$), 4 ($*$), 5.67 ($\times$). L_x/λ versus non-dimensional pycnocline thickness $h_2/(h_1+h_2)$. Symbols joined by a solid/dashed line denote stable/unstable observations respectively.

flow is assumed to be strictly horizontal and invariant. A perturbation is added to the invariant background flow and a linear stability analysis which utilizes spectral techniques is employed to analyze the perturbation. The perturbation is assumed to have a complex propagation speed, $c_p = c_r \pm i|c_i|$, for a given wavenumber k, where c_r is the propagation speed of the perturbation and $k|c_i|$ is the growth rate of the perturbation. Note that the analysis in this section (and the subsequent presentation of results) are computed in a fixed (or stationary) frame of reference i.e. the wave moves through the frame of reference with a speed c. The wave number giving the maximal growth rate is identified and the maximum growth rate is defined at this wave number by $\gamma = (k|c_i(k)|)_{max}$. Following Fructus *et al.* (2009), the unstable perturbations are assumed to undergo an amplification e^F, where F is estimated to be $F = L_x\gamma/2|c_i|$.

The convergence of data from the linear stability analysis is checked by varying the resolution of (i) the linear stability code and (ii) the steady state code (which provides

the invariant background flow). Resolutions of $n_y = 128, 256, 512$ and 1024 are compared for the linear stability code. To three decimal places, it is found that a resolution of 512 is sufficient to see convergence in all parameters presented and so $n_y = 512$ is fixed in the linear stability code throughout. Figure 15 shows the sensitivity of the stability analysis to the resolution of the steady state code for a case in which $h_2/(h_1 + h_2) = 0.286$ and $h_3/(h_1 + h_2) = 4.285$ (values chosen for comparative purposes with Fructus *et al.* (2009) given below). The subfigures of figure 15 are plotted with respect to the wave amplitude $\mathcal{A} = \eta_{rms}$ and c_0 is the linear long wave speed. The different symbols correspond to different values of the resolution (n_x, n_y) of the steady state numerical solver. Squares, downward triangles and upward triangles correspond to $(n_x, n_y) = (512, 64), (1024, 128)$, and $(2048, 256)$, respectively. By comparing the triangles it can be seen that the difference in the data sets at resolutions of $(n_x, n_y) = (1024, 128)$ and $(2048, 256)$ are negligible compared with differences between these data sets and the data set at the lower resolution (squares). Hence a resolution of $(n_x, n_y) = (1024, 128)$ (for the steady state code) is used throughout the paper unless state otherwise.

In Fructus *et al.* (2009), experimental observation of a breaking ISW with $h_2/(h_1 + h_2) = 0.286$, $h_3/(h_1+h_2) = 4.285$ and $a_1/(h_1+h_2) = 1.59 \pm 0.04$ showed that close to the wave maximum the shear-induced billows have a wavelength of $\lambda_i = 7.9h_2$ and a speed of $c_r = 0.13c_0$. Fructus *et al.* (2009) also performed a linear stability analysis of their fully nonlinear numerical results. They matched their numerical solution to the experimental observation by comparing the wave amplitude, wave speed and wave-induced horizontal velocity field in the stable part of the experimental wave. Their stability analysis predicted that, for the same values of the layer depths as measured in the experiments, the most unstable mode had a wavelength of $\lambda_i = 7.6h_2$ and a speed of $c_r = 0.13c_0$.

In figure 16 results from the linear stability analysis of Fructus *et al.* (2009) are com-

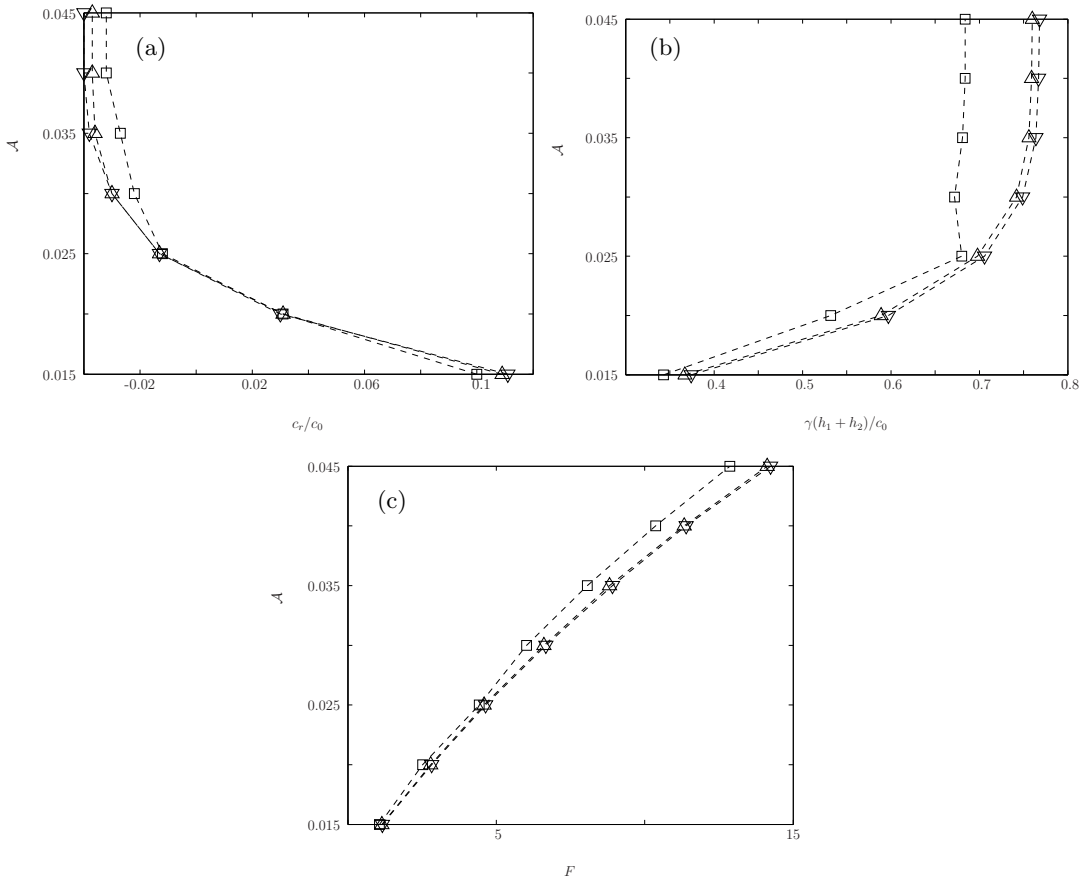

FIGURE 15. Wave amplitude $\mathcal{A}$ versus (a) billow propagation speed c_r/c_0, (b) billow growth rate $\gamma(h_1+h_2)/c_0$ and (c) amplification factor F. $h_2/(h_1+h_2) = 0.286$ and $h_3/(h_1+h_2) = 4.285$. $(n_x, n_y) = (512, 64)$ ($\square$), $(n_x, n_y) = (1024, 128)$ ($\triangledown$), $(n_x, n_y) = (2048, 256)$ ($\triangle$). Values are plotted for the perturbation with maximum temporal growth rate.

pared with the linear stability analysis performed here for a wave with the same values of $h_2/(h_1+h_2)$ and $h_3/(h_1+h_2)$ in both cases, and $a_1/(h_1+h_2)$, and δ varying as shown. The parameter δ, defined to be two grid lengths in the y direction, is a smoothing parameter which dictates how sharp the undisturbed pycnocline is (see §3.1). In the fully nonlinear simulations of Fructus *et al.* (2009) a layered approach was taken and matching conditions were employed at the discontinuous boundaries. The pycnocline in Fructus *et al.* (2009) can be thought of as being infinitely sharp ($\delta \to 0$). In order to

compare with their work, δ is varied between values of $\delta = 0.0025$ (x), 0.005 ($\triangle$) and 0.01 (*) in figure 16. When $\delta = 0.0025$ a vertical resolution of $n_y = 256$ is required to ensure the Brunt-Väisälä frequency field squared is sufficiently smooth throughout the domain in the steady state numerical code (see §3.1). Hence in figure 16, a resolution of $(n_x, n_y) = (2048, 256)$ is used to compute the steady states for the three data sets presented.

The subfigures of figure 16 show that (a) the billow propagation speed, (b) the billow growth rate, (c) the amplification factor and (d) the billow wavelength are all functions of the wave amplitude and the smoothing distance δ (the sharpness of the pycnocline). In particular, figure 16 (a) shows that as δ decreases (the pycnocline is sharpened) the propagation speed of a billow at onset increases. Moreover, there is a linear relationship between wave amplitude and billow propagation speed with increases in wave amplitude resulting in decreases in billow propagation speed. Note also that the billow propagation speed can change sign with variance in the amplitude of the wave. Figure 16 (b) shows that as δ decreases (the pycnocline is sharpened) the growth rate of a billow at onset increases. Moreover, there is a linear relationship between wave amplitude and billow growth rate with increases in wave amplitude resulting in increases in billow growth rate. Finally figure 16 (d) shows that as δ decreases (the pycnocline is sharpened) and as the wave amplitude increases the wavelength of a billow at onset decreases. A comparison of the scale on the horizontal axes of figures 16 (a), 16 (b) and 16 (d) respectively, shows that the billow propagation speed and growth rate are significantly more sensitive to changes in δ and $a_1/(h_1 + h_2)$ than the billow wavelength is. Reasonable agreement with the results of Fructus *et al.* (2009) is seen throughout.

Barad & Fringer (2010) also presented a linear stability analysis of their model. In their work F is equivalently defined as $F = \max(\sigma_i)T_w/|1 - c_r/c_p|$ where $\max(\sigma_i)$ is

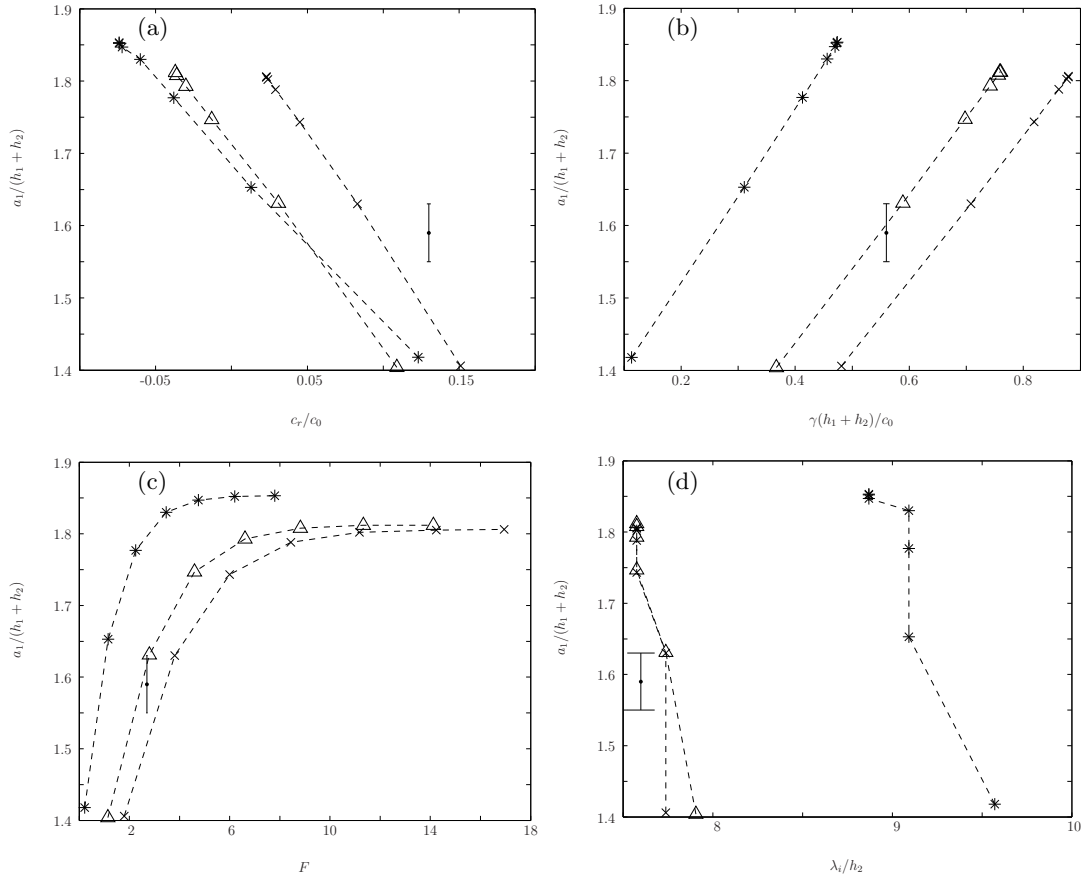

FIGURE 16. Non-dimensional amplitude $a_1/(h_1+h_2)$ versus (a) billow propagation speed c_r/c_0, (b) billow growth rate $\gamma(h_1+h_2)/c_0$, (c) amplification factor F and (d) billow wavelength λ_i/h_2. $h_2/(h_1+h_2) = 0.286$ and $h_3/(h_1+h_2) = 4.285$. The different symbols correspond to different values of the smoothing distance $\delta = 0.0025$ (x), 0.005 ($\triangle$), 0.01 (*). The black dot and associated vertical error bar is taken from Fructus *et al.* (2009). Values are plotted for the perturbation with maximum temporal growth rate.

the maximum growth rate and T_w, is the period in which parcels of fluid are subjected to $Ri < 1/4$. Barad & Fringer (2010) and Troy & Koseff (2005) predicted that ISWs and progressive interfacial wave trains respectively, will develop instabilities when the non-dimensional growth rate exceeds a critical value of $\bar{\sigma}_c T_w = 5$, where $\bar{\sigma}_c$ is the critical average growth rate over T_w. Barad & Fringer (2010) suggest that a critical bound

of $\bar{\sigma}_c T_w = 1$ can be inferred from the data presented in Fructus *et al.* (2009). They hypothesize that the smaller threshold in Fructus *et al.* (2009) may be due to disturbances present in the laboratory. However, figure 16 (c) shows that F is sensitive to the sharpness of the pycnocline (δ) and the amplitude of the wave. In addition, it was shown in §4.2 that the stability of the system is very sensitive to the structure of the background stratification. Barad & Fringer (2010) did not take account of such variations and hence the differences in thresholds between their work and that of Fructus *et al.* (2009) is more likely to be due to differences in the structure of the undisturbed density field.

For completeness, figure 17 is included to show how (a) the billow propagation speed, (b) the billow growth rate and (c) the billow wavelength vary respectively, with $h_2/(h_1 + h_2)$ and $h_3/(h_1 + h_2)$ for the same data set as in figures 9 to 12. They show that as the non-dimensional pycnocline thickness is increased the critical billow propagation speed required for instability increases (after an initial small decrease) while the critical billow growth rate and wavelength required for instability decrease. Moreover, as the non-dimensional thickness of the lower layer increases the critical billow propagation speed required for instability tends to decrease while the critical billow growth rate and wavelength required for instability increase respectively. A thorough investigation of how the non-linear billow characteristics vary with background stratification and wave amplitude is beyond the scope of the current paper. This issue will be addressed in a forthcoming paper in which a combined laboratory and numerical study will investigate the structure, evolution and mixing properties of shear-induced billows in ISWs. Note that Barad & Fringer (2010) presented three-dimensional simulations which indicated that the primary instability in their work was two-dimensional. The same result is envisaged here and hence the stability bounds presented in §4.2 and figure 17 are expected to be representative at the point of onset of instability.

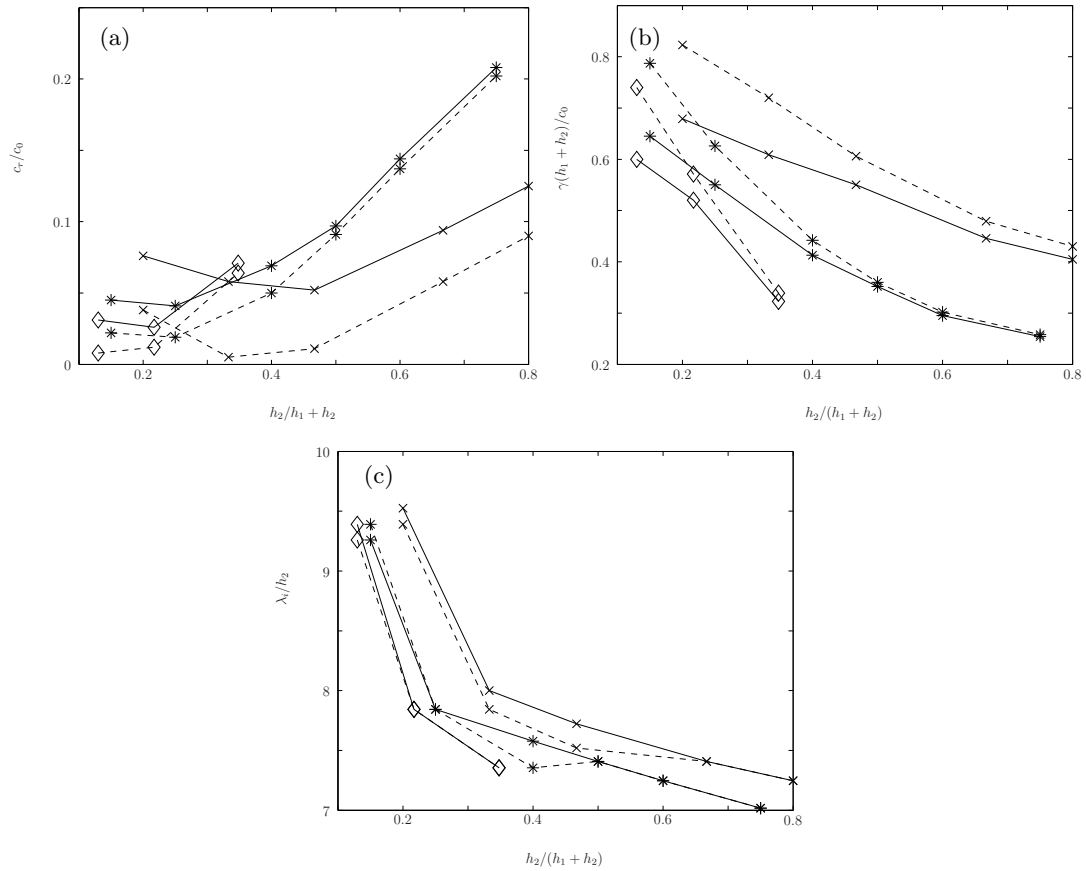

FIGURE 17. Stability diagram for different values of the lower layer thickness, $h_3/(h_1+h_2) = 3.35$ ($\diamond$), 4 ($*$), 5.67 ($\times$). (a) billow propagation speed c_r/c_0, (b) billow growth rate $\gamma(h_1+h_2)/c_0$ and (c) billow wavelength λ_i/h_2 versus non-dimensional pycnocline thickness $h_2/(h_1+h_2)$. Symbols joined by a solid/dashed line denote stable/unstable observations respectively. Values are plotted for the perturbation with maximum temporal growth rate.

6. Summary and Discussion

A numerical method for simulating shear-induced instabilities in an ISW has been presented. The work focused on ISWs propagating in a three-layer fluid in which a linearly stratified pycnocline was sandwiched between homogeneous top and bottom layers. The results showed that the stability of an ISW is very sensitive to the ratio of the layer depths in the background stratification and the sharpness in transition between the three

layers. In particular, it was shown that the critical amplitude and Richardson number required for instability are functions of $h_2/(h_1+h_2)$ and $h_3/(h_1+h_3)$, where h_1, h_2, and h_3 are the thicknesses of the upper, middle and lower layers respectively. Hence it was shown that a condition for instability based solely on a minimum Richardson number, as suggested by Barad & Fringer (2010) for example, is not sufficient. It was shown, in general, that a bound for stability, whether it be based on wave amplitude, Richardson number or any other suitable parameter, is always a function of the undisturbed background stratification. Similar results have been found for parallel shear flows dating back to the work of Miles & Howard (1964). A summary can be found in Turner (1980).

Moum *et al.* (2003) have observed unstable ISWs propagating shoreward over Oregon's continental shelf. By assuming streamlines parallel to isopycnals, they were able to infer velocity profiles from which they concluded shear-induced instabilities were the cause of the unsteadiness in their waves. The background parameters for the unstable waves that they observed were $h_2/(h_1+h_2) \approx 0.333$, $h_3/(h_1+h_2) \approx 6.267$, and $a_1/(h_1+h_2) \approx 1.333-1.667$. The numerical results presented in figure 9 suggest that the waves observed in Moum *et al.* (2003) should have been stable. However, the background stratification in Moum *et al.* (2003) was multilayered and the waves did not propagate into quiescent flow. In the numerical simulations the background fields were three layered and quiescent. Both of these differences are expected to have a significant affect on the stability of the system and hence may explain the discrepancy between the numerical simulations and the observations of Moum *et al.* (2003).

Another significant point to note in the observations of Moum *et al.* (2003) is that the wave-induced horizontal velocity was close to the wave speed. In such instances, so called convective instability is expected to be present. Convective instability in ISWs takes the form of small-scale overturning, and it has been shown in the laboratory that

it may aid shear-induced instability in ISWs, see Carr *et al.* (2008). For convective instability to occur the Brunt-Väisälä frequency must be non zero. A configuration like that presented here but in which the Brunt-Väisälä frequency is nonzero in the upper layer was considered in King *et al.* (2010). It is well known that the steady state form of ISWs propagating in such a configuration can have closed streamlines associated with them (Brown & Christie 1998; Fructus & Grue 2004). Open questions remain on how such closed streamlines should be modelled, see Helfrich & White (2010) and King *et al.* (2010). A detailed numerical and experimental study of this problem is proposed as future work with a view to understanding how convective instability may effect ISWs in the ocean.

The authors are grateful for support from the UK Engineering and Physical Sciences Research Council under its Mathematical Sciences Programme (grant number EP/F030622/1). The authors would like to thank three anonymous referees whose constructive criticisms have led to improvements in the paper.

REFERENCES

Apel, J. R., Ostrovsky, L. A., Stepanyants, Y. A. & Lynch, J. F. 2006 Internal solitons in the ocean. *Tech. Rep.*. Woods Hole Oceanog. Inst.

Apel, J. R., Ostrovsky, L. A., Stepanyants, Y. A. & Lynch, J. F. 2007 Internal solitons in the ocean and their effect on underwater sound. *J. Acoust. Soc. Am.* **121**, 695–722.

Armi, L. & Farmer, D. M. 1988 The flow of mediterranean water through the strait of gibraltar. *Prog. Oceanogr.* **21**, 1.

Barad, M. F. & Fringer, O. B. 2010 Simulations of shear instabilities in interfacial gravity waves. *J. Fluid Mech.* **644**, 61–95.

Benjamin, T. B. 1966 Internal waves of finite amplitude and permanent form. *J. Fluid Mech.* **25**, 241–270.

Brown, D. J. & Christie, D. R. 1998 Fully nonlinear solitary waves in continuously stratified incompressible boussinesq fluids. *Phys. Fluids* **10(10)**, 2569–2586.

Carr, M., Fructus, D., Grue, J., Jensen, A. & Davies, P. A. 2008 Convectively induced shear instability in large amplitude internal solitary waves. *Phys. Fluids* **20**, 12660.

Dritschel, D. G. & Ambaum, M. H. P. 1997 A contour-advective semi-lagrangian numerical algorithm for simulating fine-scale conservative dynamical fields. *Quart. J. Roy. Meteorol. Soc.* **123**, 1097–1130.

Dritschel, D. G. & Fontane, J. 2010 The combined lagrangian advection method. *J. Comput. Phys.* **229**, 5408–5417.

Fontane, J. & Dritschel, D. G. 2009 The hypercasl algorithm: a new approach to the numerical simulation of geophysical flows. *J. Comput. Phys.* **228**, 6411–6425.

Fructus, D., Carr, M., Grue, J., Jensen, A. & Davies, P. A. 2009 Shear-induced breaking of large internal solitary waves. *J. Fluid Mech.* **620**, 1–29.

Fructus, D. & Grue, J. 2004 Fully nonlinear solitary waves in a layered stratified fluid. *J. Fluid Mech.* **505**, 323–347.

Garrett, C. 2003*a* Internal tides and ocean mixing. *Science.* **301**, 1858–1859.

Garrett, C. 2003*b* Mixing with latitude. *Nature.* **422**, 477–478.

Grue 2006 *Waves in geophysical fluids-tsunamis, rogue waves, internal waves and internal tides*, 1st edn., pp. 205–270. Springer.

Grue, J., Jensen, A., Rusås, P. O. & Sveen, J. K. 2000 Breaking and broadening of internal solitary waves. *J. Fluid Mech.* **413**, 181–217.

van Haren, H. & Gostiaux, L. 2010 A deep-ocean kelvin-helmholtz billow train. *Geophys. Res. Lett.* **37**, L030605.

Hazel, P. 1972 Numerical studies of the stability of inviscid stratified shear flow. *J. Fluid Mech.* **51(1)**, 39–61.

Helfrich, K. R. & Melville, W. K. 2006 Long nonlinear internal waves. *Annu. Rev. Fluid Mech.* **38**, 395–425.

Helfrich, K. R. & White, B. L. 2010 A model for large-amplitude internal solitary waves with trapped cores. *Nonlin. Processes Geophys.* **17**, 303–318.

King, S. E., Carr, M. & Dritschel, D. G. 2010 The steady state form of large amplitude internal solitary waves. *J. Fluid Mech.* **666**, 477–505.

Lamb, K. G. 2002 A numerical investigation of solitary internal waves with trapped cores formed via shoaling. *J. Fluid Mech.* **451**, 109–144.

Lamb, K. G. & Farmer, D. 2011 Instabilities in an internal solitary-like wave on the oregon shelf. *J. Phys. Oceanogr.* **41**, 67–87.

Long, R. R. 1965 On the boussinesq approximation and its role in the theory of internal waves. *Tellus* **17**, 46–52.

Marmorino, G. O. 1990 Turbulent mixing in a salt finger staircase. *J. Geophy. Res.* **95**, 12983–12994.

Miles, J. W. & Howard, L. N. 1964 Note on a heterogeneous shear flows. *J. Fluid Mech.* **20**, 331–336.

Moum, J. N., Farmer, D. M., Smyth, W. D., Armi, L. & Vagle, S. 2003 Structure and generation of turbulence at interfaces strained by internal solitary waves propagating shoreward over the continental shelf. *J. Phys. Oceanogr.* **33**, 2093–2112.

Munk, W. & Bills, B. 2007 Tides and the climate: Some speculations. *J. Phys. Oceanogr.* **37**, 135–147.

Munk, W. & Wunsch, C. 1998 Abyssal recipes. part ii. energetics of tidal and wind mixing. *Deep-Sea Res.* **45**, 1977–2010.

Osborne, A. R. & Burch, T. L. 1980 Internal solitons in the andaman sea. *Science.* **208**, 451–460.

Osborne, A. R., Burch, T. L. & Scarlet, R. I. 1978 The influence of internal waves on deep water drilling. *J. Petroleum Technol.* **30**, 1497–1504.

Schiermeier, Q. 2007 Churn churn churn. *Nature.* **447**, 522–524.

Thorpe, S. A. 2004 Recent developments in the study of ocean turbulence. *Annu. Rev. Earth Planet. Sci.* **32**, 91–109.

Troy, C. D. & Koseff, J. R. 2005 The instability and breaking of long internal waves. *J. Fluid Mech.* **543**, 107–136.

Turkington, B., Eydeland, A. & Wang, S. 1991 A computational method for solitary internal waves in a continuously stratified fluid. *Stud. Appl. Math.* **85**, 93–127.

Turner, J. S. 1980 *Buoyancy effects in fluids*. Cambridge University Press.

Woods, J. D. 1968 Wave-induced shear instability in the summer thermocline. *J. Fluid Mech.* **32**, 791–800.

Yih, C-S 1960 Exact solutions for steady two-dimensional flow of a stratified fluid. *J. Fluid Mech.* **9**, 161–174.